RSC Advances

PAPER

View Article Online
View Journal | View Issue

Cite this: *RSC Adv.*, 2018, **8**, 14434

Raman photostability of off-resonant gap-enhanced Raman tags

Yuqing Gu,[a] Yuqing Zhang,[a] Yi Li,[*b] Xiulong Jin,[a] Chengjun Huang,[*c] Stefan A. Maier[bd] and Jian Ye[*ae]

Surface-enhanced Raman scattering (SERS) nanoprobes show promising potential for biosensing and bioimaging applications due to advantageous features of ultrahigh sensitivity and specificity. However, very limited research has been reported on the SERS photostability of nanoprobes upon continuous laser irradiation, which is critical for high-speed and time-lapse microscopy. The core–shell off-resonant gap-enhanced Raman tags (GERTs) with built-in Raman reporters, excited at near-infrared (NIR) region but with a plasmon resonance at visible region, allow decoupling the plasmon resonance behaviors with the SERS performance and therefore show ultrahigh Raman photostability during continuous laser irradiation. In this work, we have synthesized five types of off-resonant GERTs with different embedded Raman reporters, numbers of shell layer, or nanoparticle shapes. *Via* thorough examination of time-resolved SERS trajectories and quantitative analysis of photobleaching behaviors, we have demonstrated that double metallic-shell GERTs embedded with 1,4-benzenedithiol molecules show the best photostability performance, to the best of our knowledge, among all SERS nanoprobes reported before, with a photobleaching time constant up to 4.8×10^5 under a laser power density of 4.7×10^5 W cm^{-2}. Numerical calculations additionally support that the local plasmonic heating effect in fact can be greatly minimized using the off-resonance strategy. Moreover, double-shell BDT-GERTs are highly potential for high-speed and high-resolution Raman-based cell bioimaging.

Received 15th March 2018
Accepted 12th April 2018

DOI: 10.1039/c8ra02260g

rsc.li/rsc-advances

The surface-enhanced Raman scattering (SERS) effect strongly boosts the Raman signal of reporter molecules adsorbed on the surface of metallic plasmonic nanoparticles with the intense electromagnetic field enhancement.[1–7] With the unique fingerprint spectral feature, SERS nanoprobes, namely, metallic nanoparticles together with molecules as Raman reporters, have been extensively investigated for the biomedical applications including biosensing and bioimaging similar to the fluorescent nanoprobes.[8–14] In contrast to fluorophores, SERS nanoprobes exhibit a much larger multiplexing capability due to the narrow spectral linewidth. In addition, SERS nanoprobes show better stability than fluorophores since fluorophores easily suffer the photobleaching issue caused by modification of covalent bonds or non-specific reactions between the fluorophores and surrounding molecules upon singlet state-triplet state transition,[15,16] which is especially problematic in time-lapse microscopy.[17] Typically the photobleaching in SERS nanoprobes does not follow this process and is much less problematic than that in fluorophores. It can be further minimized by decreasing the laser power and prolonging the laser exposure time. However, the photobleaching is still not favorable for high-contrast SERS-based bioimaging, which recently shows great potential for intraoperative precise identification of tumor margins and microscopic tumor invasion[18–21] and inevitably requires high-speed and a number of imaging cycles.

Recently a new type of SERS nanoprobes, namely, gap-enhanced Raman tags (GERTs), have been reported to show excellent SERS enhancement,[7,22,23] which is favorable for high-speed SERS imaging.[13,22,24] GERTs are composed of plasmonic Au core–shell nanomatryoshka structures[25–27] with a uniform and nanometer-sized interior gap between the metallic core and the shell in addition to an external mesoporous silica layer if needed.[22] Such nanoprobes show strong near-infrared (NIR) Raman enhancement due to the combined near-field electromagnetic and chemical enhancement in the subnanometer core–shell junction geometry while they only present one localized surface plasmon resonance (LSPR) in the visible range in the far-field spectrum.[27] Therefore GERTs with the built-in nanogap geometry allow decoupling the LSPR spectrum with

[a]*State Key Laboratory of Oncogenes and Related Genes, School of Biomedical Engineering, Shanghai Jiao Tong University, Shanghai, P. R. China. E-mail: yejian78@sjtu.edu.cn*

[b]*The Blackett Laboratory, Department of Physics, Imperial College London, London SW7 2AZ, UK. E-mail: yi.li@imperial.ac.uk*

[c]*R&D Center of Healthcare Electronics, Institute of Microelectronics, Chinese Academy of Sciences, Beijing, P. R. China. E-mail: huangchengjun@ime.ac.cn*

[d]*Chair in Hybrid Nanosystems, Faculty of Physics, Ludwig-Maximilians-Universität München , 80799 München, Germany*

[e]*Shanghai Key Laboratory of Gynecologic Oncology, Ren Ji Hospital, School of Medicine, Shanghai Jiao Tong University, Shanghai, P. R. China*

the SERS performance. This off-resonance NIR excitation strategy is able to minimize the excitation laser induced photothermal effect to GERTs, leading to their ultrahigh SERS photostability during 30 min continuous cell and tumor SERS imaging without being photobleached.[22] The off-resonant NIR GERTs as imaging probes are also favorable for generating minimal photothermal damage to the biological samples during the imaging process, as demonstrated by monitoring the changes in mitochondrial membrane potential of cancer cells during imaging.[28] The core–shell structure of GERTs additionally offers a variety of embedded Raman reporters and the numbers of shell layer,[29] but it remains a question and a challenge to understand how these factors of nanoprobe composition and morphology affect their SERS photostability.

In this work, we synthesized five types of off-resonant GERTs either with different embedded Raman reporters (including 1,4-benzenedithiol (BDT), 4,4′-biphenyldithiol (BPDT), 4,4′-terphenyldithiol (TPDT), and 4-nitrobenzenethiol (NBT)), numbers of shell layer, or nanoparticle (NP) shapes. We have compared their particle morphologies, optical properties, and SERS photostability under continuous laser irradiation. Careful examination of time-resolved SERS trajectories and quantitative analysis of photobleaching behaviors indicate that double metallic-shell GERTs embedded with BDT molecules show the best photostability performance to the best of our knowledge. Numerical calculations are additionally performed to estimate the local laser-induced lattice temperature change of GERTs at on-resonance and off-resonance conditions. Further investigations of Raman-based cell imaging have demonstrated that those double-shell GERTs are great nanoprobes for high-speed and high-resolution Raman bioimaging.

Experimental section

Materials and instrumentation

CTAC (99%) was received from J&K Chemical Ltd (Shanghai, China). Chloroauric chloride ($HAuCl_4 \cdot 4H_2O$) was obtained from Sinopharm Chemical Reagent Co. Ltd (Shanghai, China). Ascorbic acid (>99%) was purchased from Aladdin (China). 1,4-Benzenedithiol (BDT, 98%) was acquired from TCI (Tokyo, Japan). 4-Nitrobenzenethiol (NBT) was received from Sigma-Aldrich (Shanghai, China). Silver nitrate ($AgNO_3$, >99%) was obtained from Alfa Aesar (Shanghai, China). All materials were used as received without any further purification. Nanopure water (18.2 MΩ) was used for all experiments. UV-Vis extinction spectra were measured from a UV1900 UV-Vis spectrophotometer (Aucybest, Shanghai, China). Transmission electron microscopy (TEM) images were collected on a JEM-2100F transmission electron microscope (JEOL, Tokyo, Japan) operated at 200 kV.

Synthesis of GERTs

Single-shell BDT-decorated GERTs (BDT-GERTs), BPDT-decorated GERTs (BPDT-GERTs) and TPDT-decorated GERTs (TPDT-GERTs) were prepared according to the protocols presented in our preceding work except for the increasing adsorption time of Raman reporters from 20 minutes to 3 hours for BDT-GERTs. Double-shell BDT-decorated GERTs (double-shell BDT-GERTs) were also synthesized in accordance with our previous work with some minor adjustments. First, the obtained BDT-GERTs were first centrifuged to reduce the concentration of CTAC from 50 mM to 10 mM. Second, the amount ratio of BDT-GERTs and 1,4-BDT alcoholic solution (4 mM) was 20 : 1, and the incubation time was 30 minutes. Third, the Raman reporter modified BDT-GERTs were resuspended in CTAC of 50 mM after the washing process. Fourth, the growth solution of double gold shell consisted of 9 mL CTAC (50 mM), 450 μL $HAuCl_4$ (4.86 mM) and 1200 μL ascorbic acid (40 mM). NBT-decorated GERTs (NBT-GERTs) were prepared by the method proposed in our published paper. The synthesized 10 mL Nanorods (NRs) were mixed with 300 μL NBT alcoholic solution (2 mM) under vigorous sonication, followed by the incubation for 30 minutes at 50 °C. Next, the mixture was washed three times and dispersed in 100 mM CTAC solution. Then, 200 μL $AgNO_3$ solution (100 mM) was added into 4 mL functionalized NRs with 12 mL H_2O, followed by the addition of four times molar excess of ascorbic acid. After the synthesis of GERTs, mesoporous silica coating was applied to all five types of particles based on the procedures described in our previous work.

Photostability measurements of GERTs

Raman measurements were performed on a LabRAM XploRA INV system (Horiba, China) to analyze the photostability characteristics of various GERTs. 6 μL samples (0.2 nM) were drop-cast on a silicon wafer and dried before measurement. Continuous irradiation with a 785 nm laser was applied to all five types of GERTs, with 15 minutes for NBT-GERTs and 30 minutes for the other four samples. All Raman spectra were normalized to the laser power, the exposure time, and the concentration of Raman reporters. Photobleaching time constant is obtained by fitting the decay curve to the equation $I = Ae^{(-t/\tau)}$ after evaluation of three different locations on the substrate.

Calculations of plasmonic heating effect

The plasmonic photothermal heating of the GERT by laser irradiation during the Raman measurement was calculated by coupling the Radio Frequency module with Heat Transfer module in Comsol Multiphysics (version 4.4).[30] In order to validate our numerical method in the air-silicon interfaces, modelling results in the water environment have been compared with the ref. 30 and 31. The temperature dependent parameters of Au, Si, and silica were taken from the Comsol material library. The refractive index of the embedded Raman reporter was set as 1.6 based on our previous investigation.[32]

Cell culture and Raman imaging

The HeLa cell line was purchased from Cell library of the Chinese Academy of Sciences (Shanghai, China) and cultured in a Dulbecco's modified Eagle's medium (DMEM) with 10% fetal bovine serum (FBS) and antibiotics (100 μg mL^{-1} penicillin and

100 μg mL^{-1} streptomycin) (Sigma, St. Louis, MO). The cells were cultivated in 10 cm culture dishes in a water-jacketed incubator at 37 °C with 5% CO_2-humidified atmosphere. For cell Raman imaging purposes, the cells were allowed to adhere to the quartz-bottomed plates for at least 24 h and then incubated with double-shell BDT-GERTs at a final concentration of 0.02 nM for 15 h. Following the incubation, the cells were washed thoroughly with phosphate-buffered saline (PBS) and fixed with 4% paraformaldehyde for 15 minutes at room temperature. Excess paraformaldehyde was removed with PBS and then sterile water, and the samples were air-dried before SERS measurements. The Raman image of a whole cell could be acquired in a SWIFT mode within 51 s with a 10 ms exposure time per pixel (51 × 50 pixels, 4.7×10^5 W cm^{-2}, 100× objective lens), and the imaging time could be further reduced to 36 s with a 5 ms exposure time per pixel.

Results and discussion

We have synthesized five different types of GERTs, either with different embedded Raman reporter molecules, shell thicknesses, or nanoparticle (NP) shapes using the slightly modified procedures we described before.[22,28] Fig. 1a shows the schematic illustration of GERTs and the corresponding molecular structures of embedded Raman reporters: (i) single-shell 1,4-benzenedithiol-decroated GERTs (BDT-GERTs), (ii) 4,4′-biphenyldithiol-decorated GERTs (BPDT-GERTs), (iii) 4,4′-terphenyldithiol-decorated GERTs (TPDT-GERTs), (iv) double-shell 1,4-benzenedithiol-decroated GERTs (double-shell BDT-GERTs), and (v) 4-nitrobenzenethiol-decorated GERTs (NBT-GERTs). BDT, BPDT, and TPDT are selected because they have similar molecular structures but with different molecular chain lengths. NBT is selected also because of a similar structure and with a much larger Raman cross section.[33] BDT-GERTs, BPDT-GERTs, TPDT-GERTs, and double shell BDT-GERTs all have a spherical shape but the former three have only a single-layer metallic shell. NBT-GERTs have a rodlike NP shape. All NPs are coated with a mesoporous silica layer in order to have a better bio-compatibility and the capability of further bio-functionalization. Fig. 1b shows the representative transmission electron microscopy (TEM) images of all GERTs, which indicates that all NPs are well dispersed and isolated without aggregation. Each NP has an external silica layer of around 15 nm in thickness and its mesoporous morphology is clearly observed. The Raman reporter molecule has a great impact on the gap morphology of inside the GERTs. From our previous work,[27] we have well confirmed that BDT molecule can lead to a uniform gap in single-shell GERTs with a gap size of ~0.7 nm. Very similarly, BPDT can also form a uniform internal gap in BPDT-GERTs with a slightly larger gap size of ~0.8 nm because it has a slightly longer molecular length than BDT (Fig. 1b(ii)).[32] However, the gap becomes discontinuous for TPDT-GERTs when the molecular length of the Raman reporter further increases (Fig. 1b(iii)). This is probably because of that TPDT molecules are not rigid structures and may form various orientations, therefore resulting in an uneven molecular layer on Au cores. For double-shell BDT-GERTs, the gap structure appears indistinct due to the increased thickness of the Au shell and the total particle size up to around 120 nm, relatively larger than others (Fig. 1b(iv)). More interestingly, we have no observation of the gap morphology between the Au core and the Ag shell in rodlike NBT-GERTs (Fig. 1b(v)), which is consistent to the results previously reported.[28] This important feature has been confirmed before by the high-resolution TEM but without a clear explanation yet.[28,34] The corresponding high-resolution inverted TEM images of GERTs are shown in the insets of Fig. 1a, which further confirm the observation of the gap morphology above.

The photographs in Fig. 1c show typical colors of the corresponding five GERTs (i–v): blue, pink, purple, red, and green, respectively. UV-Vis extinction spectra in Fig. 1c indicate only one localized surface plasmon resonance (LSPR) peak from the visible to NIR range for all samples. Single-shell spherical GERTs typically have a single LSPR in the range of 540–560 nm. For example, single-shell BDT-GERTs, BPDT-GERTs, and TPDT-GERTs exhibit a LSPR at 553, 541, and 551 nm, respectively. Their difference is most likely due to the variation of particle size, particle shape, and gap morphology. NBT-GERTs show a LSPR at 663 nm, which is mainly determined by the aspect ratio of NPs and the thickness of Ag shell.[28] Double-shell BDT-GERTs present the LSPR at 656 nm and their spectral linewidth is much broader than that of the other four samples because of the polydispersed particle size and the irregular shape effect. We have observed that a slight redshift (typically, 3–5 nm) of the LSPR occurs after the coating of mesoporous silica layer for all but NBT-GERTs due to the increase of the refractive index around the NPs. It can be also noted that all samples except double-shell BDT-GERTs are entirely under off-resonance condition relative to the NIR excitation laser wavelength (785 nm, indicated by the dashed line in Fig. 1c) used in the Raman measurement in this work, which is favorable for biomedical applications with a large penetration depth. In contrast, double-shell BDT-GERTs are under slightly off-resonance condition (their LSPR maximum is even around 130 nm far away from the excitation wavelength 785 nm), since they still show moderate absorption at 785 nm.

SERS photostability measurements were performed on solid GERTs drop-cast on a silicon substrate under continuous laser irradiation for 30 min with a laser power density of 3×10^5 W cm^{-2}. This test condition is more challenging than most of biological environment SERS nanoprobes applied in, such as buffer media and biological tissue, where the environmental media absorbs a part of light. All GERTs deposited on the Si substrate may randomly form aggregations, but it should be also noted that all GERTs used in this work are coated with a mesoporous silica layer with an average shell thickness of 15 nm, which keeps all NPs on the Si substrate with a dielectric distance of at least 30 nm between the metal–metal surfaces. This indicates that the LSPR of GERTs on the substrate is weakly affected by the state of NPs (*e.g.*, aggregation), since the LSPR coupling is a near-field effect.[35,36] Therefore, all GERTs on the substrate maintain the off-resonance condition relative to 785 nm excitation wavelength even when some aggregations form. This is also very similar to the situation of performing

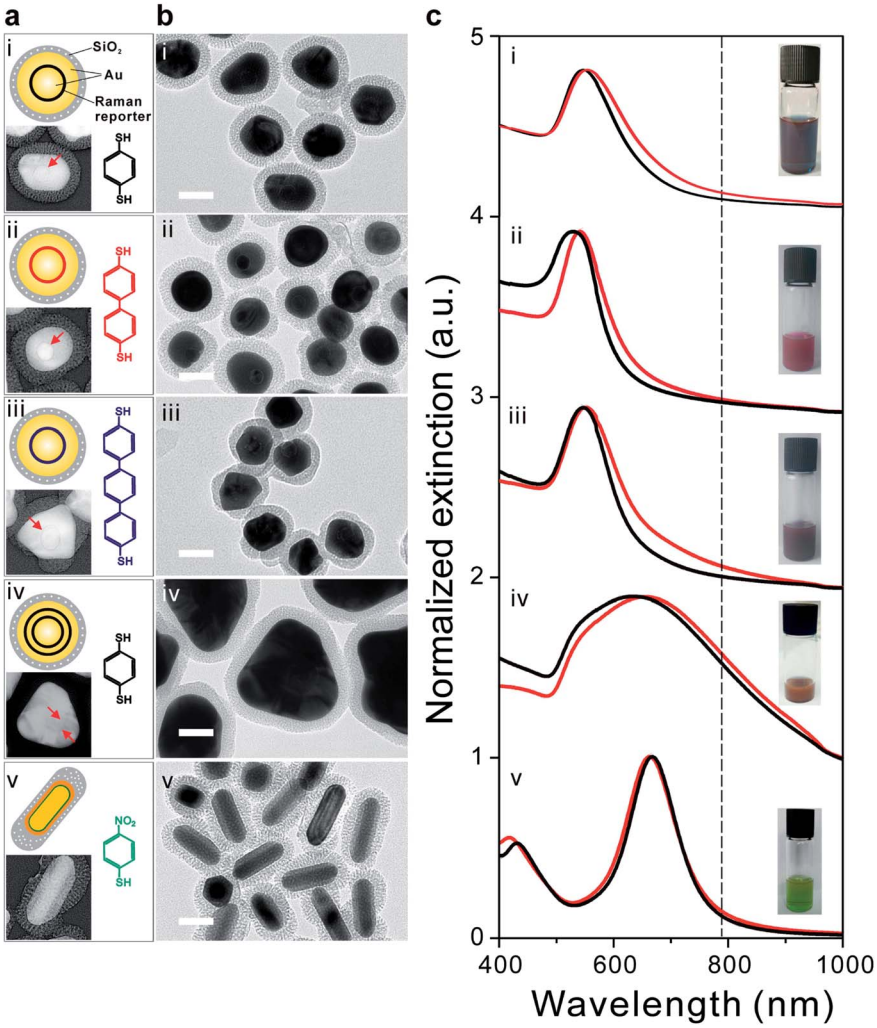

Fig. 1 Structures and optical properties of five off-resonant GERTs: (i) BDT-GERTs, (ii) BPDT-GERTs, (iii) TPDT-GERTs, (iv) double-shell BDT-GERTs, and (v) rodlike NBT-GERTs. (a) Schematic illustration of nanoparticles, inverted TEM image of nanoparticles, and molecular structure of Raman reporters. (b) TEM images of GERTs. All scale bars are 50 nm. (c) Extinction spectra of GERTs before (black) and after (red) silica coating. Dashed line indicates the laser wavelength (785 nm) used in the Raman measurements. Insets in panel c are the corresponding photos of aqueous GERTs solutions.

SERS cell imaging, where GERTs as nanoprobes are internalized by cells and form aggregations inside the cell. Raman spectra were collected every 2 s using a 785 nm laser and a 60× objective lens. All spectra were background-subtracted and their intensities were normalized to the exposure time, laser power, and concentration of embedded Raman reporters. From bright-field photo images of five types of solid GERTs on silicon wafer (Fig. 2a), negligible changes have been found before (top) and after (bottom) 30 min continuous laser irradiation. This indicates an improved photostability of GERTs stabilized by the mesoporous silica than Au nanospheres functionalized by other stabilizing agents (*e.g.*, rhodamine 6G, cetyltrimethylammonium chloride) we have reported before.[22] Fig. 2b presents time-resolved SERS trajectories of five types of GERTs. Three notable Raman bands from BPDT-GERTs and TPDT-GERTs at 1080, 1277, and 1585 cm^{-1} are ascribed to the vibrational mode of C–S stretching (ν_1 mode), C–C stretching (ν_{8a} mode), and stretching of C–C connecting the phenyl rings, respectively (Fig. 2b(ii) and (iii)).[37–39] Two strong characteristic Raman bands of single-shell and double-shell BDT-GERTs at 1055 and 1555 cm^{-1} and one weak band at 1178 cm^{-1} correspond to the phenyl-ring breathing mode (C–H in-plane bending and C–S stretching), the phenyl-ring stretching motion (8a vibrational mode), and the CH bending motion (9a vibrational mode), respectively (Fig. 2b(i) and (iv)). In close agreement with previous findings,[28,40,41] the SERS spectra of NBT-GERTs are dominated by ν (C–S) at 1081 cm^{-1}, ν (NO_2) at 1338 cm^{-1}, and ν (C–C) at 1569 cm^{-1} (Fig. 2b(v)). Although obvious SERS signals remain after continuous laser irradiation, we find different photostability behaviors of all GERTs in this work. Raman intensity of single-shell BDT-GERTs gradually decreases and remains about 60% of the initial signal during 30 min irradiation. It is worth noting that the single-shell BDT-GERTs in this work show a slight degradation of SERS

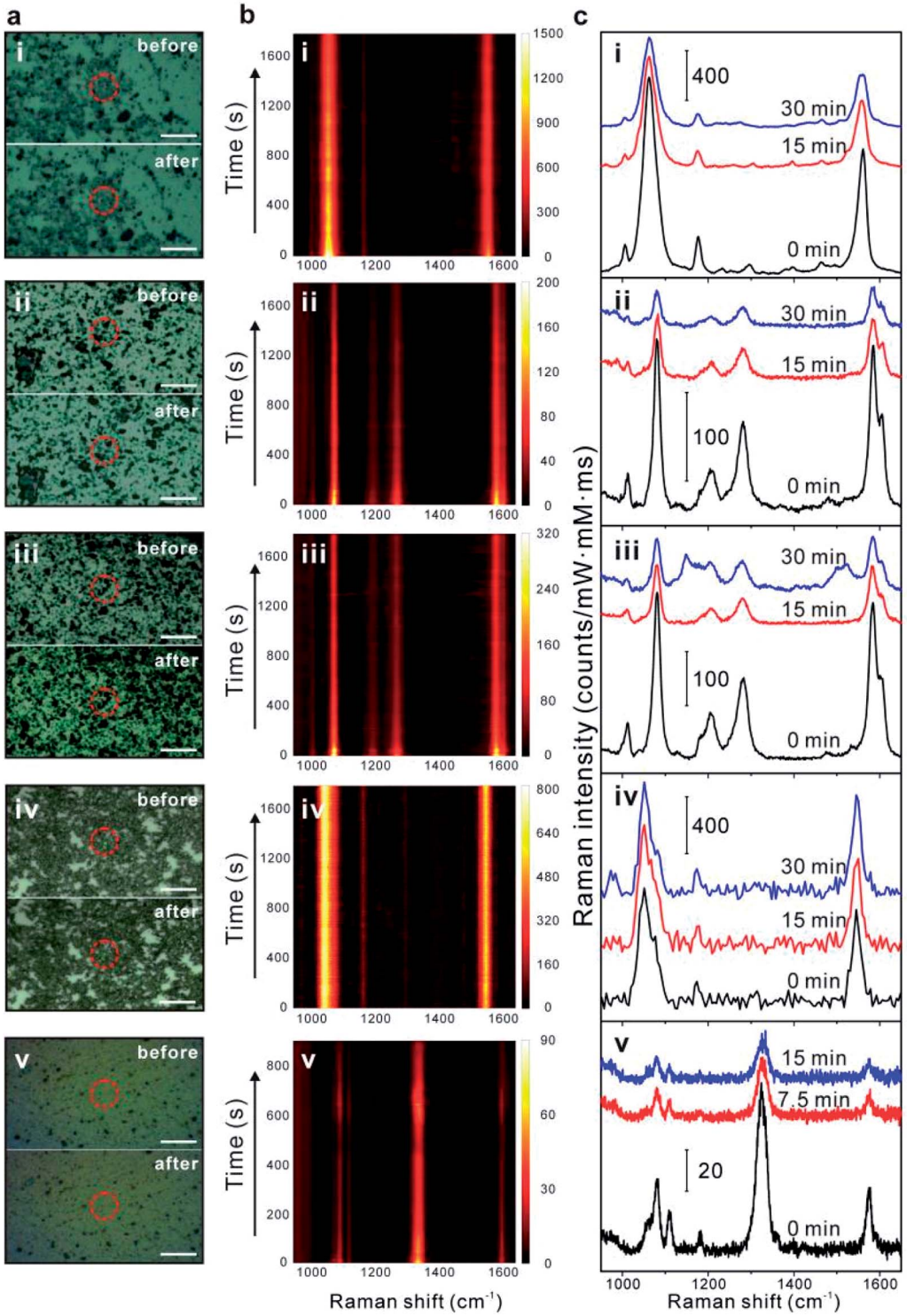

Fig. 2 SERS photostability measurements of five off-resonant GERTs: (i) BDT-GERTs, (ii) BPDT-GERTs, (iii) TPDT-GERTs, (iv) double-shell BDT-GERTs, and (v) NBT-GERTs. (a) Bright-field images of solid GERTs on a silicon wafer before (top) and after (bottom) 15 min continuous irradiation for NBT-GERTs and 30 min for the other four samples. The red circles indicate the positions where laser illuminates. All scale bars are 10 μm. (b) Time-resolved SERS spectra of solid GERTs on a silicon wafer during continuous laser irradiation for BDT/BPDT/TPDT-GERTs (30 min, 3×10^5 W cm^{-2}), double-shell BDT-GERTs (30 min, 4.7×10^5 W cm^{-2}) and NBT-GERTs (15 min, 3×10^5 W cm^{-2}). (c) Three representative SERS spectra at selected irradiation times in panel b.

photostability compared with our previous results.[22] BPDT-GERTs and TPDT-GERTs exhibit pronounced Raman signals at the initial stage but a rapid diminish occurs after around 2 min; three notable Raman bands remain on the trajectory after 30 min irradiation. NBT-GERTs provide faster but unstable decays where the SERS signal does not always decrease

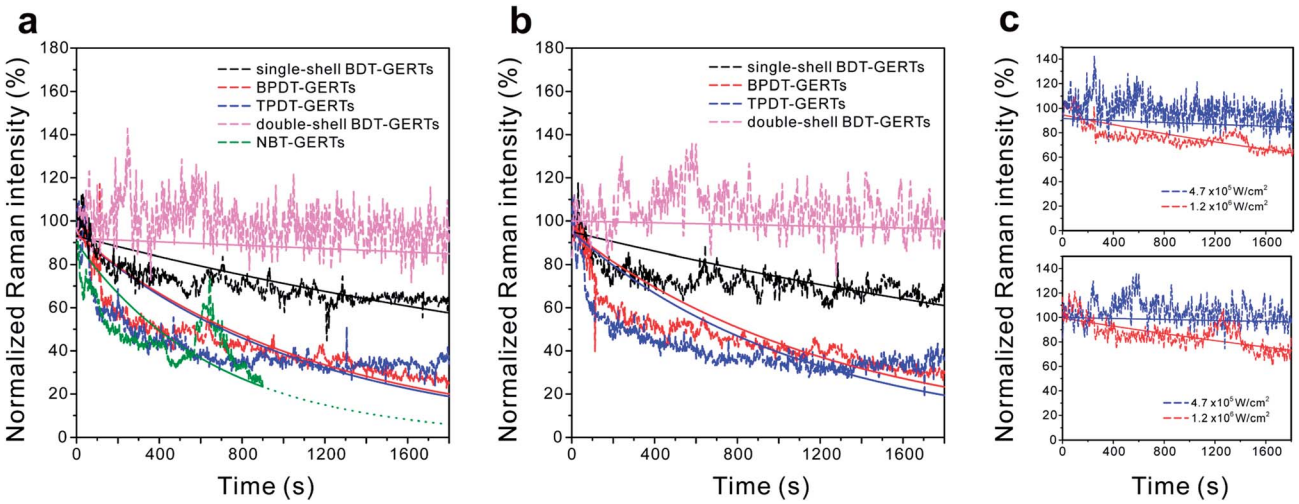

Fig. 3 Comparison of SERS photostability of different off-resonant GERTs. Time-dependent variation of integrated area of Raman bands for BPDT-GERTs ((a) 1080 cm^{-1}; (b) 1585 cm^{-1}), TPDT-GERTs ((a) 1080 cm^{-1}; (b) 1585 cm^{-1}), single-shell BDT-GERTs ((a) 1055 cm^{-1}; (b) 1555 cm^{-1}), double-shell BDT-GERTs ((a) 1055 cm^{-1}; (b) 1555 cm^{-1}), and rodlike NBT-GERTs ((a) 1338 cm^{-1}). (c) Photostability of double-shell BDT-GERTs (top: 1055 cm^{-1} band, bottom: 1555 cm^{-1} band) under different laser power densities. All solid curves are obtained by fitting the decay curves to the equation $I = Ae^{(-t/\tau)}$.

monotonically during 15 min irradiation. In contrast, double-shell BDT-GERTs show extraordinary photostability without any noticeable Raman blinking or fluctuation phenomena during 30 min irradiation. This can be explained by the fact that the metallic shell can not only enhance the SERS signal but also protect the reporter molecules from the oxygen and moisture and avoid possible desorption, which was demonstrated previously.[22] Their photostable SERS properties can be additionally demonstrated by the three representative SERS spectra, recorded before, in the middle of, and after irradiation, with almost negligible change (Fig. 2c(iv)). The representative SERS spectra from the other four samples clearly indicate a remarkable signal weakening after the irradiation (Fig. 2c(i)–(iii) and (v)). We emphasize that such extraordinary photostability of double-shell BDT-GERTs is highlighted with a large laser power density of 4.7×10^5 W cm^{-2} and an ultrashort integration time of 10 ms per spectrum, which is greatly favorable for SERS-based cell bioimaging.

Quantitative analysis of the photostability of all GERTs is carried out by plotting their photobleaching behaviors after normalization. As shown in Fig. 3a and b, the integrated areas of Raman bands at 1080 and 1585 cm^{-1} for BPDT and TPDT, 1055 and 1555 cm^{-1} for BDT, and 1338 cm^{-1} for NBT were selected as representative for investigating the photobleaching behaviors from their time-resolved SERS spectra in Fig. 2. We have find out different photobleaching time constants (τ) from these GERTs (see Table 1), which is obtained by fitting the SERS decay curves to the equation $I = Ae^{(-t/\tau)}$ (solid lines).[42] The time constants obtained are 1054 and 1003 s for BPDT-GERTs (Raman bands of 1080 and 1585 cm^{-1}), 1290 and 1526 s for TPDT-GERTs (Raman bands of 1080 and 1585 cm^{-1}), 5623 and 7628 s for single-shell BDT-GERTs (Raman bands of 1055 and 1555 cm^{-1}), 22 271 and 48 686 s for double-shell BDT-GERTs (Raman bands of 1055 and 1555 cm^{-1}), respectively. It is first-time demonstrated that the photobleaching time constant of SERS nanprobes can reach a value larger than 4.8×10^5. Although all GERTs are operated in the off-resonant conditions, distinct photobleaching behaviors of GERTs can be observed: (1) the length of Raman reporters – a better photostability of BDT-GERTs than BPDT- and TPDT-GERTs, where a shorter molecular length forms a more rigid and dense monolayer. It can be also reasonably understood that more C–C bonds with a lower bond energy (compared to C=C and C–H)[43] connecting the benzene rings exist in the molecular structure (such as TPDT) with increased benzene ring, which produces more possibilities of molecular decomposition due to the breaking of C–C bond. (2) The layer of the shells – a better photostability of double-shell GERTs than single-shell GERTs, where metallic shell protection and isolation of Raman reporters reduce the plausible interactions with the surrounding environment; (3) the type of vibrational Raman bonds – a better photostability of

Table 1 Raman photobleaching time constants of various GERTs[a]

Samples	τ_1[b] [s]	τ_2[c] [s]
BDT-GERTs	5623	7628
BPDT-GERTs	1054	1003
TPDT-GERTs	1290	1526
NBT-GERTs	667	
Double-shell BDT-GERTs[d]	22 271	48 686
Double-shell BDT-GERTs[e]	4488	5866

[a] All measurements are performed with a laser power density of 3×10^5 W cm^{-2} except for double-shell BDT-GERTs. [b] τ_1 is obtained by fitting the Raman band of 1055 cm^{-1} for BDT-GERTs and double-shell BDT-GERTs, 1080 cm^{-1} for BPDT-GERTs and TPDT-GERTs, and 1338 cm^{-1} for NBT-GERTs. [c] τ_2 is obtained by fitting the Raman band of 1555 cm^{-1} for BDT-GERTs and double-shell BDT-GERTs, 1585 cm^{-1} for BPDT-GERTs and TPDT-GERTs. [d] Measurements are performed with a laser power density of 4.7×10^5 W cm^{-2}. [e] Measurements are performed with a laser power density of 1.2×10^6 W cm^{-2}.

the phenyl-ring C–C stretching mode (1555 cm^{-1} for BDT, 1585 cm^{-1} for BPDT and TPDT) than the C–S stretching mode (1055 cm^{-1} for BDT, 1080 cm^{-1} for BPDT and TPDT), where the closed-loop structure of the phenyl ring is more conservative than the single C–S bond under continuous irradiation. Surprisingly, the photobleaching time constant of NBT-GERTs (1338 cm^{-1}) is only around 667 s, which is in line with the fact that the oxidization of the Ag shell in NBT-GERTs easily occurs during the continuous laser illumination and causes the dramatic decrease of SERS signal. We have previously demonstrated that the mesoporous silica shell plays a certain role to some extent in improving the photostability of the GERTs.[22] But the photostability result of NBT-GERTs herein implies that the oxygen still possibly penetrates through the mesoporous silica layer and consequently accelerates the oxidization under the laser illumination. We further increase the laser power density up to 1.2×10^6 W cm^{-2} to examine the photostability of double-shell BDT GERTs. Their photobleaching time constants significantly decline to 4488 and 5866 s for the Raman bands at 1055 and 1555 cm^{-1} (Fig. 3c), respectively. We also notice that the fitting of decay curves can be further improved by utilizing a two-exponential mode[44] and more investigation will be performed in future work.

It is essential to understand the contributions from plasmonic heating in the SERS photobleaching effect.[42,45–49] Accordingly, we performed numerical calculations using the commercial Comsol Multiphysics to examine the local temperature variation (ΔT) of GERTs induced by laser excitation under the on-resonance and off-resonance conditions at room temperature. Fig. 4 shows the calculated heat source density and increased temperature of a GERT (Au core: 25 nm in diameter, gap size: 0.7 nm, Au shell: 16 nm in thickness, and silica shell: 12 nm in thickness) on a Si substrate excited by a laser with a power density of 3×10^5 W cm^{-2}. The non-radiative decay of absorbed optical energy is concentrated in the internal Au core–shell with a maximal value of 3.8×10^{18} W m^{-3} at on-resonance (532 nm) condition. Followed by resistive (ohmic) heating, the lattice temperature elevation of the GERT (including the silica layer) seems to reach beyond 900 K and is highly localized in a volume close to the NP. This surprisingly high temperature is reasonable due to 15 folds less thermal conductivity in the air, which facilitates fast photobleaching during the conventional SERS measurement with a large power density in ambient atmosphere. The lattice temperature elevation of the GERT dramatically drops to merely 27 K at off-resonance condition (785 nm) and the corresponding absorbed energy also decreases to 1.0×10^{17} W m^{-3}, leading to more than one order of magnitude lower than that of on-resonance condition, which provides limited thermal effects on the gap molecules. Such significantly distinct photothermal activities are corroborated with high photostability of the off-resonant GERTs, outperforming normal on-resonant SERS nanoprobes.

Besides stable key Raman bands of GERTs, notable fluctuations of side Raman bands including the intensity variation of Raman bands and the appearance/disappearance of Raman bands have been observed during the photostability measurements of GERTs. Fig. 5a shows a number of representative SERS spectra of BPDT-GERTs during continuous measurements, for example, from 376 to 424 s, from 1160 to 1172 s, and from 1650 to 1702 s. The three main Raman bands at 1080, 1277, and

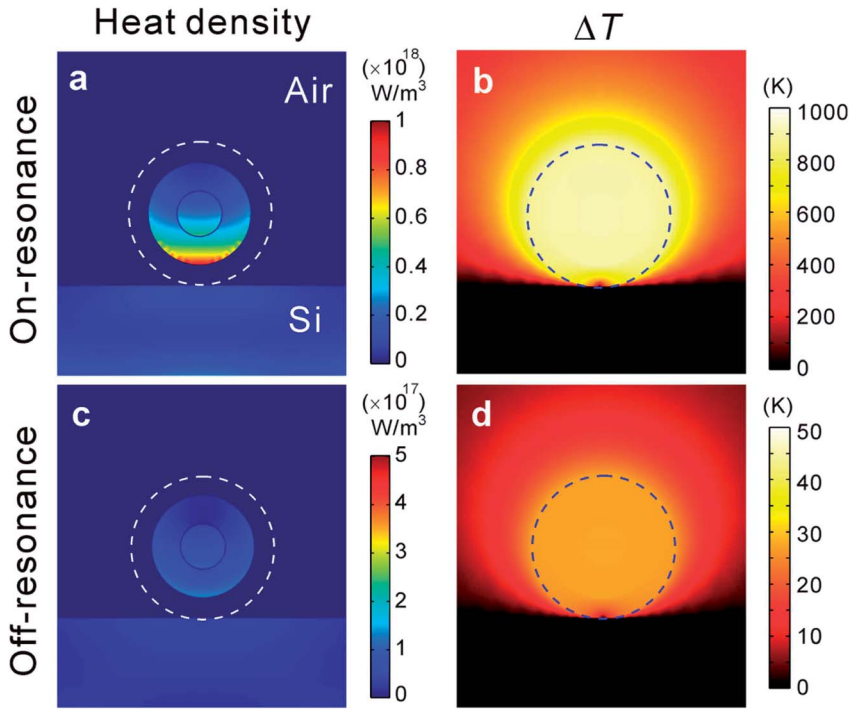

Fig. 4 Numerical calculations of plasmonic heating by laser irradiation. (a and c) Heat source density distribution and (b and d) increased temperature (ΔT) of a GERT on the Si substrate under on-resonant (532 nm) or off-resonant (785 nm) excitation with a power density of 3×10^5 W cm^{-2}. Dashed circles indicate the diameter of the GERT.

1585 cm^{-1} from BPDT are always detectable and remain constantly decreasing in general during 30 min of measurement. But Raman bands at the optical regions of 550–900 cm^{-1}, 1100–1400 cm^{-1}, and 1450–1580 cm^{-1} become variable. For example, the intensity of the Raman band at 1200 cm^{-1} continuously increases during 376–378 s and even becomes stronger than that at 1080 and 1585 cm^{-1} (two main bands) when $t = 380$ s. It can be also noticed that extra Raman bands at 679, 746, 784, 838 cm^{-1} emerge when $t = 422$ s and they suddenly disappear during the next 2 s ($t = 424$ s). Another Raman band at ~1520 cm^{-1} blinks from time to time during the measurement (Fig. 5a). Similar phenomena of Raman spectral variation can be found during the photostability test for TPDT-GERTs (Fig. 5b). For example, the Raman mode at 841 cm^{-1} unexpectedly emerges when $t = 14$ s, but becomes silent when $t = 12$, 16, 18, 20 and 22 s, and reoccurs during 268–270 and

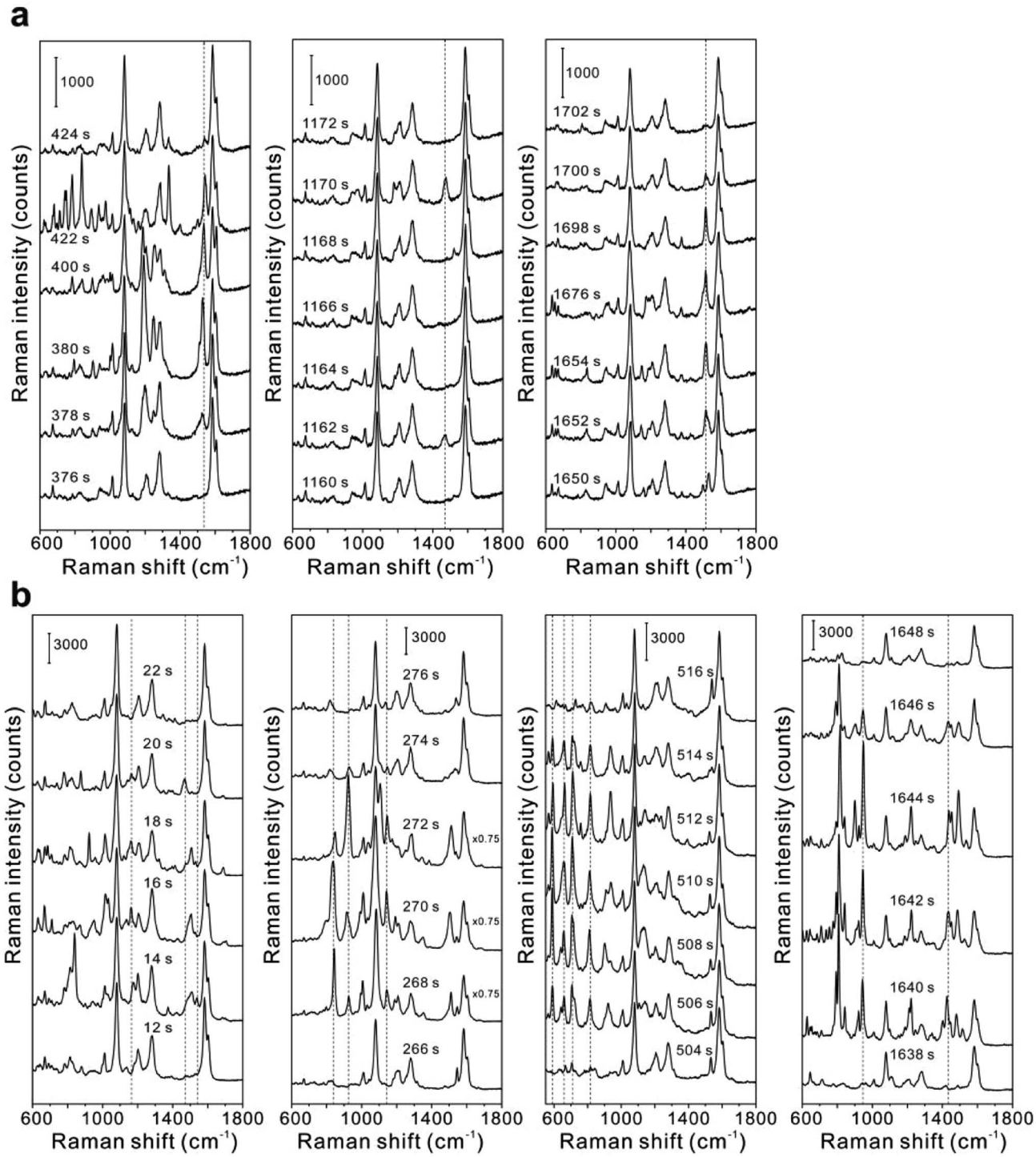

Fig. 5 SERS spectral fluctuation of (a) BPDT-GERTs and (b) TPDT-GERTs during the photostability measurements.

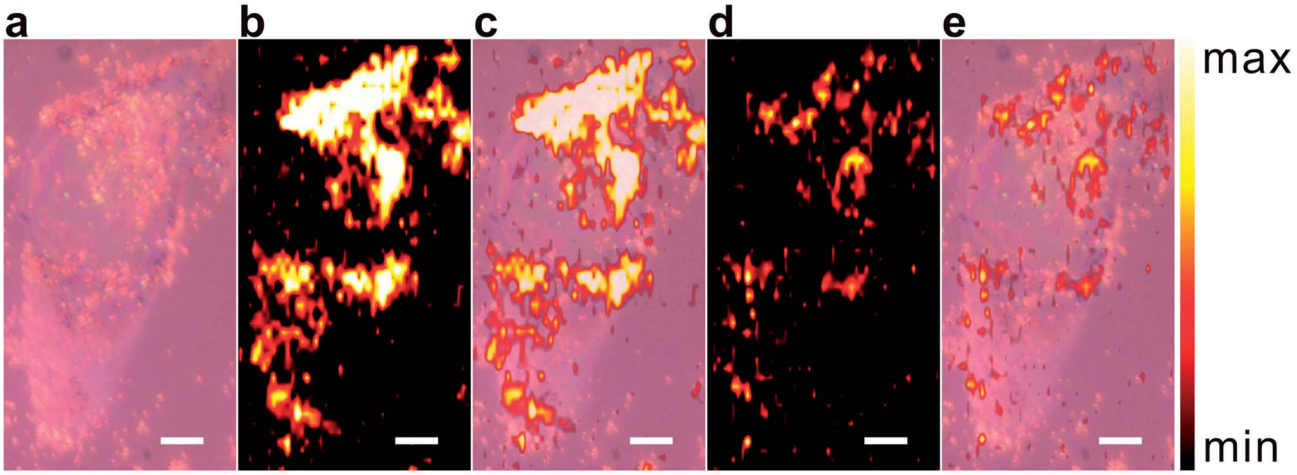

Fig. 6 Raman imaging for HeLa cells stained with double-shell GERTs. (a) Bright-field image, (b and d) Raman images and (c and e) the corresponding overlay images of a single cell. Raman images were acquired with exposure time of (b) 10 ms and (d) 5 ms per pixel, plotted using the Raman band at 1055 cm^{-1}. All scale bars are 5 μm.

1640–1646 s. Multiple vibrational modes in the range of 550–900 cm^{-1} (for example, 590, 659, 707, and 814 cm^{-1}) also appear during 506–514 s. The "blinking" effect has been previously reported in the SERS detection of single molecule mainly due to the diffusion of molecules into and out of the electromagnetic "hot spot".[4,5,50,51] However, all GERTs used in this work are solid samples on the silicon substrate, where the Raman reporters are embedded into the nanogaps of GERTs and isolated from air and moisture by metallic shell and mesoporous silica shell. After thorough examination of all these switchable Raman spectra, we found that the blinking effect is much more favorable for both BPDT-GERTs and TPDT-GERTs than BDT-GERTs. The most plausible reason is the fact that the molecular structure of BPDT and TPDT is longer and more flexible and includes more decomposable C–C bonds[43] (connecting the benzene rings) compared to BDT, more easily inducing the reorientation and decomposition of adsorbed Raman molecules during laser irradiation,[52–54] such as the variation of the torsion angle between two phenyl rings of BPDT and TPDT[52] and π–π coupling and Raman cross-sections relative to light incident direction.[34,52–54] In contrast, BDT molecule itself is simply rigid due to the double Au-thiol bounding. It should be pointed out that we cannot exclude the photo-reactions of the reporters during the irradiation process although they are completely embedded into the nanogaps of metallic nanoparticles.

Previously we have demonstrated that double-shell BDT-GERTs exhibit excellent SERS performance, even one order of magnitude stronger than single-shell BDT-GERTs.[29] Therefore, together with their ultraphotostability during laser irradiation herein, we choose double-shell BDT-GERTs as optical nanoprobes for fast cell Raman imaging. Fig. 6 shows the bright-field and Raman images of a single HeLa cell stained with double-shell BDT-GERTs. The SWIFT technology from LabRAM XploRA INV system combines the fast readout rates and enhanced signal to greatly improve Raman imaging speed and quality.[55] In our experiments, the Raman image of a single cell labeled with double-shell BDT-GERTs could be obtained within 51 s (2550 spectra acquired from an area of 28 μm × 51 μm) with an exposure time of 10 ms per pixel (Fig. 6b). The bright-field image and Raman image of the cell also coincided well in the overlay image (Fig. 6c). Moreover, we could further shorten the imaging time on a single cell with a high-resolution (51 × 50 pixels) down to 36 s at an exposure time of 5 ms per pixel (Fig. 6d and e). Such imaging capability with double-shell BDT-GERTs show great potential for high-speed and high-resolution Raman imaging of cells and tissues.

Conclusions

In summary, we have successfully prepared five types of GERTs with different embedded Raman reporters, numbers of metallic shell, and NP shapes including single-shell BDT-GERTs, BPDT-GERTs, TPDT-GERTs, double-shell BDT-GERTs, and rodlike NBT-GERTs. With a single plasmon resonance in the visible range, they all show superior off-resonant NIR SERS properties when excited by 785 nm laser. By comparing their SERS photostability under continuous laser irradiation up to 30 min with a laser power density of larger than 3×10^5 W cm^{-2}, we have concluded that double-shell BDT-GERTs show the best photostability with a photobleaching time constant up to 4.8×10^5. This is mainly attributed to the excellent protection of Raman reporters by two layers of metallic shell and the off-resonant SERS property that efficiently minimizes the plasmonic photothermal damage during the SERS measurement, which is supported by our numerical calculations. Finally, we have demonstrated that double-shell BDT-GERTs can be utilized for Raman cell bioimaging at a high speed of 36 s and a high resolution of 51 × 50 pixels.

Conflicts of interest

There are no conflicts to declare.

Acknowledgements

We gratefully acknowledge the National Natural Science Foundation of China (No. 81571763 and 81622026), Shanghai Jiao Tong University (No. YG2016MS51 and YG2017MS54) and the Grant from the Shanghai Key Laboratory of Gynecologic Oncology for their financial support.

References

1 E. C. Le Ru and P. G. Etchegoin, *Principles of Surface-Enhanced Raman Spectroscopy*, Elsevier, Amsterdam, 2009.
2 S.-Y. Ding, E.-M. You, Z.-Q. Tian and M. Moskovits, Electromagnetic theories of surface-enhanced Raman spectroscopy, *Chem. Soc. Rev.*, 2017, **46**(13), 4042–4076.
3 J. Ye, F. Wen, H. Sobhani, J. B. Lassiter, P. V. Dorpe, P. Nordlander and N. J. Halas, Plasmonic nanoclusters: near field properties of the Fano resonance interrogated with SERS, *Nano Lett.*, 2012, **12**(3), 1660–1667.
4 K. Kneipp, Y. Wang, H. Kneipp, L. T. Perelman, I. Itzkan, R. R. Dasari and M. S. Feld, Single molecule detection using surface-enhanced Raman scattering (SERS), *Phys. Rev. Lett.*, 1997, **78**(9), 1667.
5 S. Nie and S. R. Emory, Probing single molecules and single nanoparticles by surface-enhanced Raman scattering, *science*, 1997, **275**(5303), 1102–1106.
6 J. F. Li, Y. F. Huang, Y. Ding, Z. L. Yang, S. B. Li, X. S. Zhou, F. R. Fan, W. Zhang, Z. Y. Zhou and D. Y. Wu, Shell-isolated nanoparticle-enhanced Raman spectroscopy, *nature*, 2010, **464**(7287), 392–395.
7 D. K. Lim, K. S. Jeon, J. H. Hwang, H. Kim, S. Kwon, Y. D. Suh and J. M. Nam, Highly uniform and reproducible surface-enhanced Raman scattering from DNA-tailorable nanoparticles with 1-nm interior gap, *Nat. Nanotechnol.*, 2011, **6**(7), 452–460.
8 X. Qian, X.-H. Peng, D. O. Ansari, Q. Yin-Goen, G. Z. Chen, D. M. Shin, L. Yang, A. N. Young, M. D. Wang and S. Nie, In vivo tumor targeting and spectroscopic detection with surface-enhanced Raman nanoparticle tags, *Nat. Biotechnol.*, 2008, **26**(1), 83–90.
9 Y. Wang, B. Yan and L. Chen, SERS tags: novel optical nanoprobes for bioanalysis, *Chem. Rev.*, 2012, **113**(3), 1391–1428.
10 R. Panneerselvam, G.-K. Liu, Y.-H. Wang, J.-Y. Liu, S.-Y. Ding, J.-F. Li, D.-Y. Wu and Z.-Q. Tian, Surface-enhanced Raman spectroscopy: bottlenecks and future directions, *Chem. Commun.*, 2018, **54**(1), 10–25.
11 A. F. Palonpon, J. Ando, H. Yamakoshi, K. Dodo, M. Sodeoka, S. Kawata and K. Fujita, Raman and SERS microscopy for molecular imaging of live cells, *Nat. Protoc.*, 2013, **8**(4), 677–692.
12 Q. Hu, L.-L. Tay, M. Noestheden and J. P. Pezacki, Mammalian cell surface imaging with nitrile-functionalized nanoprobes: biophysical characterization of aggregation and polarization anisotropy in SERS imaging, *J. Am. Chem. Soc.*, 2007, **129**(1), 14–15.
13 J. W. Kang, P. T. So, R. R. Dasari and D.-K. Lim, High Resolution Live Cell Raman Imaging Using Subcellular Organelle-Targeting SERS-Sensitive Gold Nanoparticles with Highly Narrow Intra-Nanogap, *Nano Lett.*, 2015, **15**(3), 1766–1772.
14 S. E. Bohndiek, A. Wagadarikar, C. L. Zavaleta, D. Van de Sompel, E. Garai, J. V. Jokerst, S. Yazdanfar and S. S. Gambhir, A small animal Raman instrument for rapid, wide-area, spectroscopic imaging, *Proc. Natl. Acad. Sci. U. S. A.*, 2013, **110**(30), 12408–12413.
15 C. Eggeling, J. Widengren, R. Rigler and C. Seidel, Photobleaching of fluorescent dyes under conditions used for single-molecule detection: Evidence of two-step photolysis, *Anal. Chem.*, 1998, **70**(13), 2651–2659.
16 M. P. Gordon, T. Ha and P. R. Selvin, Single-molecule high-resolution imaging with photobleaching, *Proc. Natl. Acad. Sci. U. S. A.*, 2004, **101**(17), 6462–6465.
17 T. Bernas, J. P. Robinson, E. K. Asem and B. Rajwa, Loss of image quality in photobleaching during microscopic imaging of fluorescent probes bound to chromatin, *J. Biomed. Opt.*, 2005, **10**(6), 064015.
18 M. F. Kircher, A. de la Zerda, J. V. Jokerst, C. L. Zavaleta, P. J. Kempen, E. Mittra, K. Pitter, R. Huang, C. Campos and F. Habte, A brain tumor molecular imaging strategy using a new triple-modality MRI-photoacoustic-Raman nanoparticle, *Nat. Med.*, 2012, **18**(5), 829–834.
19 S. Harmsen, R. Huang, M. A. Wall, H. Karabeber, J. M. Samii, M. Spaliviero, J. R. White, S. Monette, R. O'Connor and K. L. Pitter, Surface-enhanced resonance Raman scattering nanostars for high-precision cancer imaging, *Sci. Transl. Med.*, 2015, **7**(271), 271ra7.
20 H. Karabeber, R. Huang, P. Iacono, J. M. Samii, K. Pitter, E. C. Holland and M. F. Kircher, Guiding brain tumor resection using surface-enhanced Raman scattering nanoparticles and a hand-held Raman scanner, *ACS Nano*, 2014, **8**(10), 9755–9766.
21 J. V. Jokerst, A. J. Cole, D. Van de Sompel and S. S. Gambhir, Gold nanorods for ovarian cancer detection with photoacoustic imaging and resection guidance *via* Raman imaging in living mice, *ACS Nano*, 2012, **6**(11), 10366–10377.
22 Y. Zhang, Y. Qiu, L. Lin, H. Gu, Z. Xiao and J. Ye, Ultraphotostable Mesoporous Silica-Coated Gap-Enhanced Raman Tags (GERTs) for High-Speed Bioimaging, *ACS Appl. Mater. Interfaces*, 2017, **9**(4), 3995–4005.
23 J. W. Oh, D. K. Lim, G. H. Kim, Y. D. Suh and J. M. Nam, Thiolated DNA-based chemistry and control in the structure and optical properties of plasmonic nanoparticles with ultrasmall interior nanogap, *J. Am. Chem. Soc.*, 2014, **136**(40), 14052–14059.
24 Z. Bao, Y. Zhang, Z. Tan, X. Yin, W. Di and J. Ye, Gap-enhanced Raman tags for high-contrast sentinel lymph node imaging, *Biomaterials*, 2018, **163**, 105–115.
25 E. Prodan, C. Radloff, N. Halas and P. Nordlander, A hybridization model for the plasmon response of complex nanostructures, *Science*, 2003, **302**(5644), 419–422.

26 V. Kulkarni, E. Prodan and P. Nordlander, Quantum plasmonics: optical properties of a nanomatryushka, *Nano Lett.*, 2013, **13**(12), 5873–5879.
27 L. Lin, M. Zapata, M. Xiong, Z. Liu, S. Wang, H. Xu, A. G. Borisov, H. Gu, P. Nordlander, J. Aizpurua and J. Ye, Nanooptics of Plasmonic Nanomatryoshkas: Shrinking the Size of a Core–Shell Junction to Subnanometer, *Nano Lett.*, 2015, **15**(10), 6419–6428.
28 X. Jin, B. N. Khlebtsov, V. A. Khanadeev, N. G. Khlebtsov and J. Ye, Rational Design of Ultrabright SERS Probes with Embedded Reporters for Bioimaging and Photothermal Therapy, *ACS Appl. Mater. Interfaces*, 2017, **9**(36), 30387–30397.
29 L. Lin, H. Gu and J. Ye, Plasmonic multi-shell nanomatryoshka particles as highly tunable SERS tags with built-in reporters, *Chem. Commun.*, 2015, **51**(100), 17740–17743.
30 G. Baffou, P. Bon, J. Savatier, J. Polleux, M. Zhu, M. Merlin, H. Rigneault and S. Monneret, Thermal imaging of nanostructures by quantitative optical phase analysis, *ACS Nano*, 2012, **6**(3), 2452–2458.
31 J. Gargiulo, T. Brick, I. L. Violi, F. C. Herrera, T. Shibanuma, P. Albella, F. G. Requejo, E. Cortés, S. A. Maier and F. D. Stefani, Understanding and Reducing Photothermal Forces for the Fabrication of Au Nanoparticle Dimers by Optical Printing, *Nano Lett.*, 2017, **17**(9), 5747–5755.
32 L. Lin, Z. Liu, X. Li, H. Gu and J. Ye, Quantifying the reflective index of nanometer-thick thiolated molecular layers on nanoparticles, *Nanoscale*, 2017, **9**(6), 2213–2218.
33 B. Mir-Simon, I. Reche-Perez, L. Guerrini, N. Pazos-Perez and R. A. Alvarez-Puebla, Universal one-pot and scalable synthesis of SERS encoded nanoparticles, *Chem. Mater.*, 2015, **27**(3), 950–958.
34 W. Shen, X. Lin, C. Jiang, C. Li, H. Lin, J. Huang, S. Wang, G. Liu, X. Yan, Q. Zhong and B. Ren, Reliable Quantitative SERS Analysis Facilitated by Core-Shell Nanoparticles with Embedded Internal Standards, *Angew. Chem.*, 2015, **54**(25), 7308–7312.
35 J. Li, J. Ye, C. Chen, Y. Li, N. Verellen, V. V. Moshchalkov, L. Lagae and P. Van Dorpe, Revisiting the surface sensitivity of nanoplasmonic biosensors, *ACS Photonics*, 2015, **2**(3), 425–431.
36 P. K. Jain, W. Huang and M. A. El-Sayed, On the universal scaling behavior of the distance decay of plasmon coupling in metal nanoparticle pairs: a plasmon ruler equation, *Nano Lett.*, 2007, **7**(7), 2080–2088.
37 Z. Ioffe, T. Shamai, A. Ophir, G. Noy, I. Yutsis, K. Kfir, O. Cheshnovsky and Y. Selzer, Detection of heating in current-carrying molecular junctions by Raman scattering, *Nat. Nanotechnol.*, 2008, **3**(12), 727–732.
38 E. O. Ganbold and S. W. Joo, Raman Spectroscopy of Biphenyl-4, 4'-dithiol and p-Terphenyl-4, 4 ″-dithiol on Gold Surfaces, *Bull. Korean Chem. Soc.*, 2015, **36**(3), 887–890.
39 Y. R. Lee, M. S. Kim and C. H. Kwon, Surface-Enhanced Raman Scattering and DFT Study of 4, 4'-Biphenyldithiol on Silver Surface, *Bull. Korean Chem. Soc.*, 2013, **34**(2), 470–474.
40 S. Hong and X. Li, Optimal size of gold nanoparticles for surface-enhanced Raman spectroscopy under different conditions, *J. Nanomater.*, 2013, **2013**, 49.
41 Y. Huang, Y. Fang, Z. Zhang, L. Zhu and M. Sun, Nanowire-supported plasmonic waveguide for remote excitation of surface-enhanced Raman scattering, *Light: Sci. Appl.*, 2014, **3**(8), e199.
42 B. Pettinger, B. Ren, G. Picardi, R. Schuster and G. Ertl, Tip-enhanced Raman spectroscopy (TERS) of malachite green isothiocyanate at Au (111): bleaching behavior under the influence of high electromagnetic fields, *J. Raman Spectrosc.*, 2005, **36**(6–7), 541–550.
43 J. E. Huheey, E. Keiter and R. Keiter, *Inorganic Chemistry*, edn 4th, HarperCollins, New York, NY, 1993.
44 R. Reisfeld, A. Weiss, T. Saraidarov, E. Yariv and A. Ishchenko, Solid-state lasers based on inorganic–organic hybrid materials obtained by combined sol–gel polymer technology, *Polym. Adv. Technol.*, 2004, **15**(6), 291–301.
45 G. Baffou, J. Polleux, H. Rigneault and S. Monneret, Super-heating and micro-bubble generation around plasmonic nanoparticles under cw illumination, *J. Phys. Chem. C*, 2014, **118**(9), 4890–4898.
46 Z. Fang, Y.-R. Zhen, O. Neumann, A. Polman, F. J. García de Abajo, P. Nordlander and N. J. Halas, Evolution of light-induced vapor generation at a liquid-immersed metallic nanoparticle, *Nano Lett.*, 2013, **13**(4), 1736–1742.
47 C. Fang, L. Shao, Y. Zhao, J. Wang and H. Wu, A gold nanocrystal/poly (dimethylsiloxane) composite for plasmonic heating on microfluidic chips, *Adv. Mater.*, 2012, **24**(1), 94–98.
48 Y. Fang, N.-H. Seong and D. D. Dlott, Measurement of the distribution of site enhancements in surface-enhanced Raman scattering, *Science*, 2008, **321**(5887), 388–392.
49 N. Harris, M. J. Ford and M. B. Cortie, Optimization of plasmonic heating by gold nanospheres and nanoshells, *J. Phys. Chem. B*, 2006, **110**(22), 10701–10707.
50 X.-M. Qian and S. Nie, Single-molecule and single-nanoparticle SERS: from fundamental mechanisms to biomedical applications, *Chem. Soc. Rev.*, 2008, **37**(5), 912–920.
51 Y. Maruyama, M. Ishikawa and M. Futamata, Thermal activation of blinking in SERS signal, *J. Phys. Chem. B*, 2004, **108**(2), 673–678.
52 L. Cui, B. Liu, D. Vonlanthen, M. Mayor, Y. Fu, J.-F. Li and T. Wandlowski, In situ gap-mode Raman spectroscopy on single-crystal Au (100) electrodes: tuning the torsion angle of 4, 4′-biphenyldithiols by an electrochemical gate field, *J. Am. Chem. Soc.*, 2011, **133**(19), 7332–7335.
53 K. T. Carron and L. G. Hurley, Axial and azimuthal angle determination with surface-enhanced Raman spectroscopy: thiophenol on copper, silver, and gold metal surfaces, *J. Phys. Chem.*, 1991, **95**(24), 9979–9984.
54 C. A. Szafranski, W. Tanner, P. E. Laibinis and R. L. Garrell, Surface-enhanced Raman spectroscopy of aromatic thiols and disulfides on gold electrodes, *Langmuir*, 1998, **14**(13), 3570–3579.
55 Horiba. http://www.horiba.com.

